RSC Advances

PAPER

View Article Online
View Journal | View Issue

Cite this: *RSC Adv.*, 2025, **15**, 34003

Efficient water capture under low humidity using Ni-modified MOF-5: scalable atmospheric water harvesting systems

Momna Aziz,[a] Raouf Hassan,[b] Muhammad Saeed-Ul-Hassan,[a] Muhammad Ehtisham,[a] Mansour S. Almatawa,[b] Ahmad K. Badawi[c] and Bushra Ismail *[a]

Atmospheric Water Harvesting (AWH) has advanced as a sustainable, energy-efficient, and cost-effective strategy to address global water scarcity. Among AWH techniques, sorption-based systems (SBAWH) offer significant advantages; however, their practical deployment is limited by the lack of efficient and scalable sorbent materials capable of high-water uptake under low to moderate relative humidity (RH) conditions. This study investigates the synthesis and performance of pristine MOF-5 and its nickel-doped derivatives (20% and 40% Ni-MOF-5), fabricated *via* a direct mixing approach, for application in SBAWH systems. The novelty of this work lies in the systematic comparison of pristine and Ni-substituted MOF-5 sorbents for enhanced water adsorption under low RH environments, an area that remains underexplored. Comprehensive material characterization was conducted using X-ray diffraction (XRD), Fourier-transform infrared spectroscopy (FTIR), scanning electron microscopy (SEM), and energy-dispersive X-ray spectroscopy (EDX) to clarify the structural and compositional attributes. Water sorption isotherms were obtained using a custom-built AWH prototype operating under controlled RH conditions (35–75%). At RH levels of 65%, 35%, and 55%, the water uptake capacities of MOF-5, 20% Ni-MOF-5, and 40% Ni-MOF-5 were 151, 162, and 142 mg g^{-1}, respectively. Thermodynamic analyses indicated that the adsorption process is spontaneous and exothermic, while isotherm and kinetic modeling confirmed a chemisorption dominated mechanism. The superior performance of 20% Ni-MOF-5, particularly under low humidity conditions, highlights its promise as a scalable and effective sorbent for next generation SBAWH systems.

Received 21st July 2025
Accepted 11th September 2025

DOI: 10.1039/d5ra05257b

rsc.li/rsc-advances

1. Introduction

Water is universally regarded as a vital prerequisite for life, underpinning ecological balance, agricultural productivity, and socioeconomic development.[1,2] Even though there is 1.3 billion km^3 of water on earth, just 3% is freshwater. Despite its abundance on Earth, only a small proportion exists as accessible freshwater, and increasing demand driven by population growth, industrialization, and agriculture has intensified global water scarcity.[3–5] By the year 2050, global freshwater availability is projected to decline dramatically, with per capita resources expected to diminish to nearly two-thirds of present levels. Estimates suggest that between 2 and 7 billion individuals could face severe difficulties in securing adequate water for their daily requirements.[6] The severity of this challenge is particularly pronounced in arid and semi-arid regions, where limited precipitation and the inherently uneven spatial distribution of finite freshwater resources exacerbate water scarcity.[7]

Several approaches have been employed to address the growing demand for freshwater, including desalination, wastewater treatment, and atmospheric water harvesting (AWH).[8–10] In arid and semi-arid regions, the implementation of conventional large-scale technologies such as desalination and reverse osmosis is often hindered by prohibitive economic costs and substantial logistical challenges, thereby limiting their viability as sustainable freshwater solutions.[11,12]

Consequently, atmospheric water harvesting (AWH) is a decentralized approach to obtain freshwater by capturing atmospheric vapor, representing nearly 13 000 trillion liters of untapped resource. This is particularly important in arid and remote regions where conventional water supplies are limited and transport infrastructure is impractical.[13,14] Current AWH

[a]*Department of Chemistry, COMSATS University Islamabad, Abbottabad Campus, 22060, Pakistan. E-mail: bushraismail@cuiatd.edu.pk; mscchem70795@gmail.com; msaeed5651123@gmail.com; muhammadEhtasham10@gmail.com; Fax: +92 992 383595; Tel: +92 992 383592*

[b]*Civil Engineering Department, College of Engineering, Imam Mohammad Ibn Saud Islamic University (IMSIU), 11432 Riyadh, Saudi Arabia. E-mail: rahassan@imamu.edu.sa; msmatawa@imamu.edu.sa*

[c]*Civil Engineering Department, El-Madina Higher Institute for Engineering and Technology, Giza 12588, Egypt. E-mail: dr.ahmedkaram91@gmail.com*

technologies include dew harvesting, fog harvesting, and sorbent-assisted systems.[15]

Dew harvesting, which relies on cooling air below its dew point to induce condensation, is a conventional method for atmospheric water collection but is energy-intensive and highly dependent on geographic and climatic conditions, thereby increasing water costs.[16,17] Fog harvesting employs mesh-based collectors to capture airborne water droplets; however, its efficacy is largely restricted to hilly and coastal regions, thereby constraining its widespread applicability.[18]

In contrast, AWH utilizes sorbents to capture water from atmosphere even at low humidity. The absorbed vapor can be released using low-grade heat or solar energy and condensed into liquid water. Owing to its adaptability and scalability, SBAWH is regarded as one of the most promising routes for sustainable freshwater generation.[19] Although widely used in AWH, silica gel[20] and zeolites[21] suffer from sluggish uptake, limited capacity at low humidity, and require high regeneration temperatures, while hygroscopic salts, despite their high water affinity, face durability issues due to agglomeration, liquid leakage, and structural degradation.[22] Table 1 shows different sorbents capacities for water harvesting with some limitations.

In the rapidly evolving landscape of materials science, Metal–Organic Frameworks (MOFs) have established themselves as one of the most versatile and promising classes of advanced materials.[27] Constructed by the coordination of metal ions or clusters with multifunctional organic linkers. MOFs exhibit highly ordered porous architectures with tunable physicochemical properties. Their exceptional surface area, structural diversity, and chemical flexibility have attracted widespread attention from chemists, physicists, and engineers alike.[28] As a result, MOFs are increasingly being explored for diverse applications, including gas storage and separation,[29] catalysis,[30] sensing,[31] photocatalysis[32] and energy storage,[33] positioning them at the forefront of next-generation functional materials. Table 2 shows adsorption capacities of different MOFs for water harvesting.

Among all other MOFs, MOF-5 (IRMOF-1) represents one of the most prototypical and extensively investigated members of the metal organic framework (MOF) family shown in Fig. 1. Structurally, it consists of a three-dimensional network formed by terephthalate linkers coordinated to Zn_4O secondary building units, and was originally synthesized by Fang and co-workers.[40] The framework is distinguished by its highly ordered architecture, adjustable pore geometry, exceptional surface area, and notable thermal stability.[41] These attributes have positioned MOF-5 as a benchmark system, underpinning its wide-ranging applications in gas adsorption and storage,[42] electrochemical energy systems,[43] heterogeneous catalysis,[44] emerging biomedical platforms,[45] sensing[46] and adsorption.[47]

Table 1 Water adsorption capacities of different sorbents for atmospheric water harvesting

Materials	Water uptake in g g^{-1}	Drawbacks	References
Alg-$CaCl_2$	1 g g^{-1}	Particles agglomerates during hydration, sometimes salt leakages issue	23
Silica gel	0.15 kg kg^{-1}	Low efficiency at low humidity, poor structural tenability	24
LiX-zeolites	0.192 g g^{-1}	Require high regeneration temperature	21
Polyacrylamide hydrogel with $CaCl_2$	1.1–1.3 g water per g gel	Salt leakage during cycling	25
Graphene oxide (GO laminate)	Up to 0.58 g g^{-1}	Performance highly RH-dependent; low uptake at very low RH	26

Table 2 Adsorption capacities of different MOFs for AWH

MOF	Adsorption capacity	RH% range	Drawbacks	Research gap	References
MOF-801	2.8 kg kg^{-1}	10–90	Monolithic form shows unexpectedly lower uptake than powder (capillary condensation effects); adsorption strongly dependent on binder type	Optimizing shaping (monoliths/composites) and binder selection to preserve adsorption efficiency	34 and 35
MIL-101 (Cr)	1 g g^{-1}	Greater than 30	Requires additional energy input for cooling Increases system design complexity and cost	Limited understanding of its long-term stability	36
MOF-303	≈0.39 g g^{-1}	20	Slow desorption kinetics and requires several hours for completion	Need for scalable processing into device-compatible forms while maintaining fast kinetics and high low-RH capacity	37 and 38
Cr-UiO-66	0.59 g g^{-1}	10–90	Better uptake, but stability in long-term cycling not fully proven	Investigate scale-up, regeneration efficiency, and integration into AWH devices	39

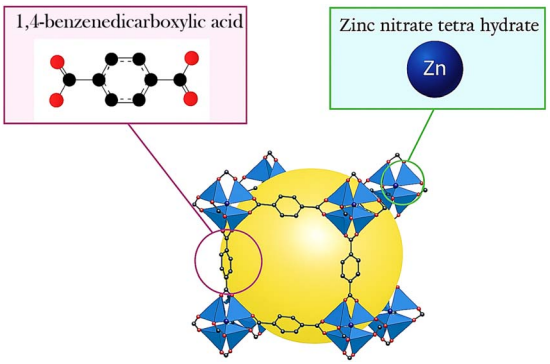

Fig. 1 Crystal structures of MOF-5 (C, black; Zn, blue; O, red; gust molecule), yellow sphere and all H atoms omitted for clarity.[41]

MOF-5 however exhibits significant moisture sensitivity under ambient conditions due to weak metal oxygen coordination, which facilitates hydrolytic attack leading to structural collapse.[48] Scientists are actively working to improve its hydrolytic stability. Recent investigations indicate that secondary metal doping in MOFs can significantly improve structural stability, generate defect sites, and facilitate synergistic adsorption pathways.[49,50]

Yang *et al.* reported that Ni(II)-doped MOF-5 nano/microcrystals with controlled morphology and size exhibit enhanced hydrostability and high surface area, with gas sorption properties strongly dependent on particle morphology and size.[51] Botas *et al.* showed that substituting Zn^{2+} with Co^{2+} in MOF-5 slightly improved H_2, CH_4, and CO_2 uptake at high pressures, though gains were limited by inaccessible metal sites.[52] Huanhuan *et al.* synthesized Ni-doped MOF-5, which showed improved hydrolytic stability, higher hydrogen uptake, and 4 day structural durability compared to undoped MOF-5.[53]

While the synthesis of MOF-5 and its metal-doped derivatives (including Ni-MOF-5) has been reported previously, most studies have primarily focused on structural characterization or gas adsorption (*e.g.*, CO_2, H_2). Reports on the systematic evaluation of water vapor adsorption under controlled humidity conditions remain scarce. In particular, the impact of Ni-doping level on moisture uptake capacity, has not been comprehensively addressed. In this work, we highlight these aspects, providing new insights into the role of Ni incorporation in tailoring the water adsorption performance of MOF-5. Despite the promising potential of MOF-5, comprehensive understanding of the effects of metal substitution, particularly Ni-doping, on SBAWH performance under low relative humidity conditions remains limited. To address this gap, the present study synthesizes and characterizes pristine MOF-5 alongside 20% and 40% Ni-doped derivatives *via* direct mixing approach, with a focus on elucidating their structural, thermodynamic, and water adsorption behaviors under controlled humidity conditions. This work unveils how Ni-doping enhances MOF-5's structure and water adsorption under low humidity, offering a promising route for efficient atmospheric water harvesting.

2. Experimental

2.1 Materials

All chemicals were highly pure, obtained from a commercial supplier, and used without any sort of extra treatment. Materials that were employed in the manufacturing of both pristine and its doped variants are zinc nitrate hexahydrate ($Zn(NO_3)_2 \cdot 6H_2O$), terephthalic acid (H_2BDC), *N*,*N*′-dimethylformamide (DMF), triethanolamine (TEA), and nickel nitrate hexahydrate ($Ni(NO_3)_2 \cdot 6H_2O$).

2.2 Synthesis of MOF-5 and Ni-doped MOF-5

Pristine MOF-5 was synthesized by adapting an earlier reported protocol, utilizing a direct mixing route with slight modifications.[54] The synthesis procedure involves 0.62 g (2.08 mmol) of zinc nitrate hexahydrate, and 0.16 g (0.96 mmol) of H_2BDC were fully dissolved in 20 mL of DMF at ambient temperature. Subsequently, 11 mL of TEA was adding dropwise with constant stirring. Then the reaction mixture was sealed and agitated for two hours at room temperature. After that, centrifugation was carried out to obtain the solid precipitates.

These solid precipitates were submerged in DMF for three days and the solvent was changed daily. Subsequently, the precipitates were washed several times with distilled water and DMF. Finally, the solid precipitates were vacuum-dried for 12 hours at 80 °C, resulting in the production of MOF-5 particles. Ni-doped derivatives of pristine material were synthesized by following the above-mentioned procedure for pure MOF-5. The synthesis of 20 Ni-MOF-5 and 40 Ni-MOF-5 was carried out by taking 0.416 mmol (0.12 g) and 0.832 mmol (0.24 g) of nickel nitrate hexahydrate and 1.664 mmol (0.50 g) and 1.248 mmol (0.38 g) of zinc nitrate hexahydrate.

2.3 Characterization

The successful synthesis of the target materials was validated through XRD, SEM, EDX, FTIR, and PZC. The crystallographic structure as well as the lattice parameters, crystal size and shape, phase composition, and orientation of the crystal planes inside the material was determined by XRD analysis, which is the analysis of the diffraction pattern formed when X-rays interact with crystalline materials. All the required parameters were evaluated on the basis of the given equations;

$$a = [d^2/(h^2 + k^2 + k^2)]^{1/2} \quad (1)$$

$$V_{\text{cell}} = a^3 \quad (2)$$

$$D = \frac{k\lambda}{\beta \cos \theta_\beta} \quad (3)$$

$$\rho_{\text{X-ray}} = \frac{ZM}{V_{\text{cell}} N_A} \quad (4)$$

The indices d, hkl, and N_A correspond to specific values for each line in the XRD pattern. K, Z, M and V_{cell} respectively, all following standard definitions. The symbol μ represents the

Bragg's angle, λ denotes the X-ray wavelength of 1.542 Å, and β indicates full width at half maximum. FTIR analysis was used to confirm the presence of functional groups. Surface morphology was determined by using SEM, while the elemental composition was evaluated by EDX analysis.

PZC is defined as a pH at which the net charge on the material surface is zero. The PZC of each sample was assessed through the salt addition technique by suspending 12.5 mg of the material in 5 mL of 0.1 M KNO_3, ensuring homogeneous dispersion. The pH was maintained at 2, 4, 6, 8, and 10 by adding a dropwise 0.1 M solution of HCl and NH_4OH. After ensuring that the pH values were maintained, each of these samples were placed on a circular orbital shaker for one day and a change of pH was recorded at the end of the day. A graph that displays the difference between the starting pH (pH_i) and the change in pH (ΔpH) was used to calculate the pH_{pzc} value. The surface exhibits a negative charge when pH exceeds pH_{pzc} (pH > pH_{pzc}) and a positive charge when pH falls below pH_{pzc} (pH < pH_{pzc}).[55]

3. Adsorption studies

An adsorption setup was used to evaluate the adsorption behavior of materials at different RH values, from 35% to 75%. The goal was to examine how the material behaved and performed when it came to moisture harvesting by changing humidity levels. This is a straightforward, enclosed device consisting of a glass barrier having 12 cm height and 10 cm width, with an installed humidifier to regulate humidity. Furthermore, a miniature fan was incorporated into the closed chamber to ensure stable regulation of both temperature and humidity throughout the experimental process.

Samples were weighed initially as they were prepared. The materials were purified by sequential washing with DI water, filtration, and drying at 80 °C in an oven until a constant weight confirmed the absence of residual moisture. All samples were subjected to testing within the atmospheric water harvesting (AWH) setup under controlled humidity conditions. Weight changes were noted after every 20 minutes until the saturation point was reached. EMC of synthesized samples was calculated at different RH ranges from 35% to 75%. Using the water vapor adsorption profiles, the EMC was evaluated by correlating the moisture content of each sample with the corresponding adsorption time. The following formula was used to calculate the moisture content (M_c), which indicates the amount of water present in a sample:

$$M_c = \frac{\text{weight of wet sample} - \text{weight of dry sample}}{\text{total weight of the sample}} \quad (5)$$

The units of measurement for moisture content are mg g^{-1} or g g^{-1}. Furthermore, moisture content data was used to explore the connection between EMC and a_w. Adsorption-isotherm models represent process efficiency, adsorption mechanisms, surface interactions, and adsorbent capacity. The effectiveness of the adsorption process was assessed using the Langmuir, Freundlich, and Temkin models. The Langmuir adsorption isotherm can be mathematically expressed as follows:

$$\frac{1}{Q_e} = \frac{1}{Q_{max} K_L} \frac{1}{C_e} = \frac{1}{Q_{max}} \quad (6)$$

The variables Q_e, C_e, K_L, and Q_{max} indicate the number of adsorbate molecules absorbed per gram of adsorbent, adsorbate equilibrium concentration, adsorbent monolayer capacity, and K_L is Langmuir constant respectively, in this equation. The following equation represents the Freundlich model:

$$\ln Q_e = \ln k_f + \frac{1}{n} \ln C_e \quad (7)$$

Within the Freundlich model, the constant k_f represents the adsorption capacity, whereas n characterizes the adsorption intensity. Temkin models of isotherm, accounting for adsorbate–adsorbent interactions, is described by the following equation

$$Q_e = B_T \quad \ln(A_T) + B_T \quad \ln(C_e) \quad (8)$$

Here, B_T corresponds to the Temkin constant related to the heat of adsorption, while A_T denotes the binding equilibrium constant.[56]

4. Kinetic studies

The kinetic characteristics of adsorption were assessed by fitting the experimental data to pseudo-first-order and pseudo-second-order models. By using the following formula, we calculated M_c at time and EMC;

$$M_t = \frac{W_t - W_O}{W_O} \times 100 \quad (9)$$

$$M_e = \frac{W_e - W_O}{W_O} \times 100 \quad (10)$$

where W_e is the sample's weight at equilibrium and W_t is the sample's weight at time t. W_O represents the sample's initial weight in grams.

As-synthesized samples were subjected to both models but the second-order kinetic functioned satisfactorily on as-synthesized materials. Pseudo 2nd order kinetics model is frequently used to explain the chemical events involved in the adsorption process. The corresponding equation can be used to calculate the equilibrium adsorption quantity, M_e.

$$\frac{t}{M_t} = \frac{1}{k_2 {M_e}^2} + \frac{1}{M_e} \quad (11)$$

where the parameter k_2 represents the adsorption rate constant, measured in units of (min^{-1}).[57]

5. Thermodynamic studies

Gibbs free energy (ΔG), entropy (ΔS), and isosteric heat of adsorption (Q_{st}) are the three thermodynamic quantities that

form the foundation of any study of thermodynamics. These equations were used to determine these parameters.

$$Q_{st} = q_{st} + H_L \quad (12)$$

$$\ln a_w = -\frac{q_{st}}{R}\frac{1}{T} + \frac{\Delta S}{R} \quad (13)$$

$$\Delta G = RT \quad \ln \quad a_w \quad (14)$$

ΔG determines whether a process is spontaneous or non-spontaneous. When ΔG is negative, it indicates a spontaneous adsorption process and *vice versa*.[58]

6. Results and discussion

The pristine MOF-5 framework, along with its Ni-doped derivatives, was successfully synthesized employing a direct mixing strategy. The obtained materials were systematically characterized using a suite of physicochemical techniques to confirm their structural integrity, crystallinity, and compositional uniformity. Furthermore, their adsorption performance was rigorously evaluated through comprehensive mathematical modeling, supported by kinetic and thermodynamic analyses, in order to elucidate the underlying adsorption mechanisms and the influence of metal substitution on the overall sorption behavior.

The XRD analysis was carried out to study the chemical composition and crystallinity of the synthesized sample as shown in Fig. 2. The observed patterns matched well with (CIF file no. 1516287) and also exhibited a close resemblance to those reported by Chinglenthoiba,[59] Rayyan Ali Shaukat,[60] Hulya[61] and Anand.[62]

MOF-5 displays intense peaks at 2θ positions given in Table 3, which match well with the standard pattern. The sharp peaks signify the elevated crystallinity of MOF-5. The absence of the ~9.8° peak can be attributed to pore filling by residual solvent or adsorbed water molecules, which alters the electron density within the framework and suppresses the corresponding diffraction reflection. This indicates that guest species occupy the pores, thereby modifying the long-range periodicity detected by XRD without necessarily disrupting the overall MOF-5 framework. The X-ray diffraction patterns of Ni-doped MOF-5 exhibit a high degree of similarity to those of the pristine MOF-5, suggesting that the fundamental crystalline framework is preserved upon nickel incorporation, thereby confirming the successful substitution of Ni into the MOF-5 structure.

Table 3 Comparison of 2theta positions of standard CIF pattern with the synthesized MOF-5 and its doped derivatives

	hkl	2theta (°)
CIF: file no. 1516287	440	19.428
	731	26.489
	751	29.940
MOF-5	440	19.321
	731	26.400
	751	29.910
20 Ni-MOF-5	440	19.311
	731	26.400
	751	29.900
40 Ni-MOF-5	440	19.321
	731	26.30
	751	29.801

For comparison, a table below shows the peak positions of all the synthesized MOF samples and compares with the data of CIF file no. 1516287. All the values match well with the reference file, indicating the formation of MOF and Ni-doped derivatives.

FTIR spectroscopy shows the presence of functional groups, molecular shape, intra and inter-interactions within the molecules. The FTIR spectra of the pure MOF-5 and its doped variants are given in Fig. 3. The tensile vibration of Zn–O in the tetrahedral coordinated ZnO_4 cluster is accountable for the peak at 528 cm^{-1}. Additionally, the out-of-plane bending vibration of the C–H bond was found at 726 cm^{-1} and 880 cm^{-1},

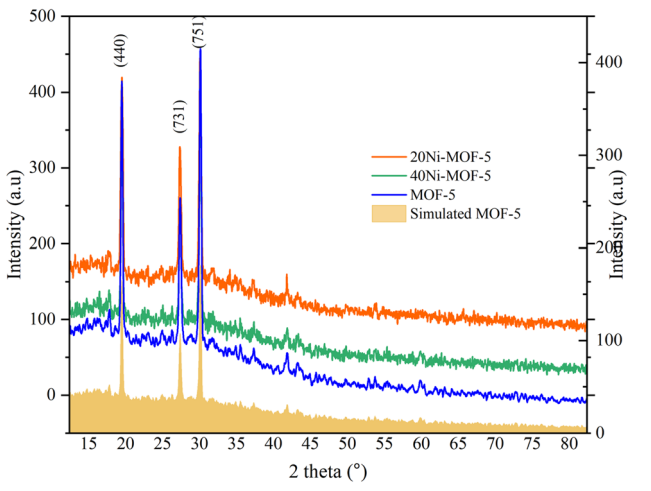

Fig. 2 XRD pattern of MOF-5 and its Ni doped derivatives.

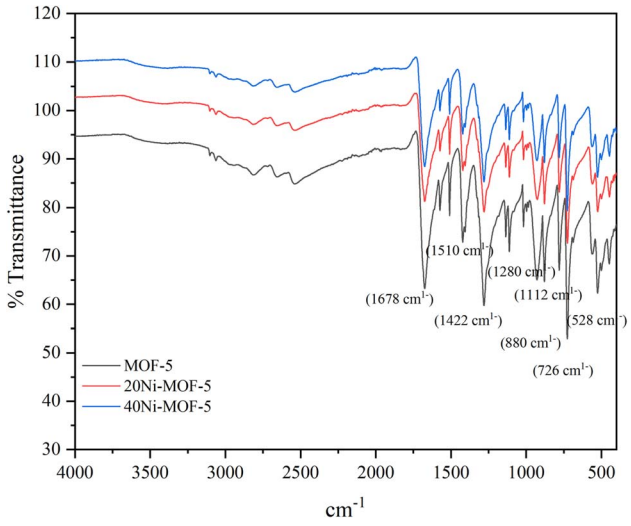

Fig. 3 FTIR graph for MOF-5 and its doped derivatives.

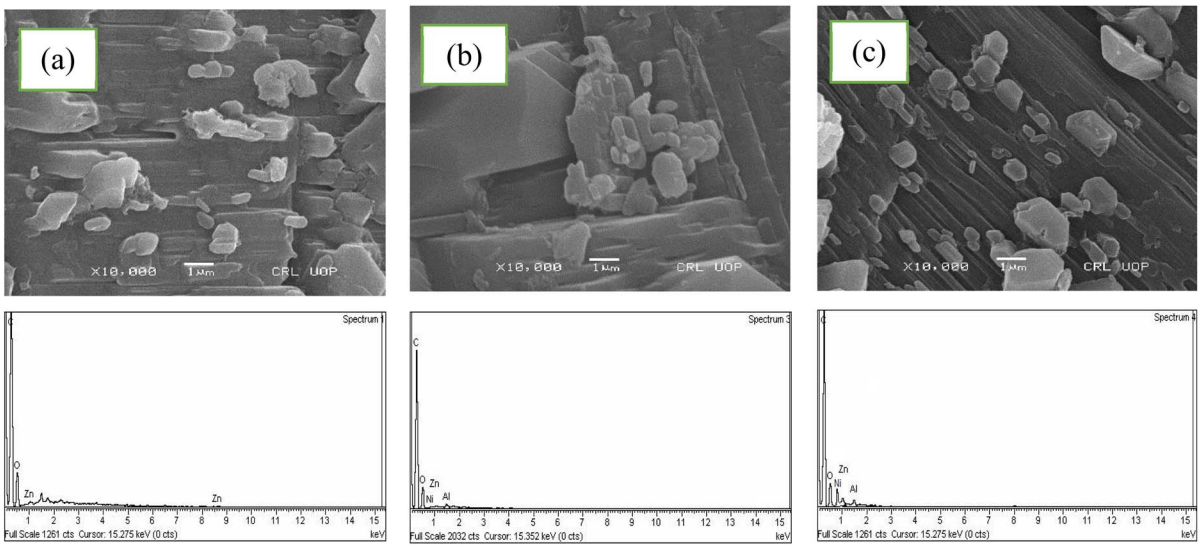

Fig. 4 SEM-EDS analysis of (a) MOF-5, (b) 20 Ni-MOF-5 and (c) 40 Ni-MOF-5 XRD and EDX analyses confirmed the successful synthesis of MOF-5 and its nickel-doped derivatives, validating the incorporation of Ni into the MOF-5 framework without compromising its crystallinity or structural integrity.

while the in-plane bending vibration of the C–H bond was found at 1112 cm^{-1} and 1280 cm^{-1}. The symmetric and asymmetric stretching vibration of the –COO bond shows strong distinctive peaks at 1422 cm^{-1}, 1510 cm^{-1}, and 1678 cm^{-1} respectively.

The morphological characteristics of samples were examined using a SEM analysis. The concentration of dopant significantly influences the surface characteristics, as shown in Fig. 4. It is observed that at lower concentrations of Ni, crystals are agglomerated and they appear as an interpenetrated crystal, while when the concentration of dopant is increased, they appear as a single crystal with cubic shape.

EDX spectroscopy gives information about elemental composition of samples. The spectra indicate the presence of Zn, C, and O in MOF-5, whereas the doped derivatives also exhibit the peak of Ni which confirms the successful synthesis of Ni-doped MOF. A small amount of Al is observed which may be due to the aluminum foil used in the preparation of the SEM sample. Ni was successfully doped into the MOF-5 structure, as evidenced by the absence of peak shifts and changes in intensity in the XRD spectra of Ni-doped MOF-5 as compared to MOF-5 spectra (Fig. 2).

The EDX spectra of both the parent and doped derivatives, shown in Fig. 4, confirm the successful doping of Ni in 20 Ni-MOF-5 and 40 Ni-MOF-5. Additionally, the peak intensity of Ni in 40 Ni-MOF-5 is higher than in 20 Ni-MOF-5, indicating a greater amount of Ni incorporation in the former. The change in pH was determined by taking the difference between the final and initial pH. Change in pH value for MOF-5 (5), 20 Ni-MOF-5 (8.5), and 40 Ni-MOF-5 (9). So, the MOF-5 surface possesses a negative charge while its doped derivatives possess a positive charge. The negative part of MOF-5 attaches to the positive part of water while the positive part of doped derivatives attaches to the negative part of water.

6.1 Moisture adsorption studies on synthesized materials

The obtained moisture adsorption data of all synthesized materials was plotted by using Origin software and MS Excel. Water adsorption experiments revealed that pristine MOF-5 exhibited an adsorption capacity of 151 mg g^{-1} at a RH of 65%. Upon doping with 20% and 40% Ni, the materials displayed adsorption capacities of 162 mg g^{-1} (at 35% RH) and 142 mg g^{-1} (at 55% RH), respectively.

Notably, the 20% Ni-MOF-5 variant showed superior performance under low humidity conditions, highlighting the synergistic effect of Ni incorporation in enhancing water uptake, particularly in arid environments. These findings suggest that controlled metal doping in MOF-5 can tune the sorption characteristics, potentially through increased defect density and modified hydrophilicity, which facilitate chemisorption dominated water capture under challenging conditions. The observed trend aligns with the hypothesis that moderate Ni substitution improves adsorption capacity and kinetics, while higher substitution levels may introduce structural distortion or pore blockage, slightly reducing performance.

The material's surface contains some adsorption-accessible sites as water molecules come towards these sites these sites are filled and the material achieves its saturation point. The saturation point is the moment at which the equilibrium state is achieved (ref. to Table 4). Equilibrium moisture content (EMC) is the state of a substance when it neither adsorbs nor desorbs moisture. The adsorption behavior of different materials at different RH (35 to 75%) is depicted in Fig. 5. Highest M_c value for MOF-5 is 151 (mg g^{-1}) at RH of 65 ± 2%, for 20 Ni-MOF-5 is 162 (mg g^{-1}) at RH of 35 ± 2% and for 40 Ni-MOF-5 is 128 (mg g^{-1}) at RH of 55 ± 2%. At initial concentration, as more spaces are available for adsorption so highest adsorption was achieved. After that, the curve shows a small decline which may be due to the filling of all vacant sites.

Table 4 Saturation point (S_p) with moisture content (M_c) of MOF-5 and its doped derivatives

	Relative humidity (%)				
	35 ± 2%	45 ± 2%	55 ± 2%	65 ± 2%	75 ± 2%
Materials	S_p (min)/M_c (mg g^{-1})	S_p (min)/M_c (mg g^{-1})	S_p (min)/M_c (mg g^{-1})	S_p (min)/M_c (mg g^{-1})	S_p (min)/M_c (mg g^{-1})
MOF-5	100/109	100/91	100/108	100/151	100/118
20 Ni-MOF-5	140/162	120/107	120/127	100/77	80/114
40 Ni-MOF-5	100/96	120/92	120/128	100/124	80/118

In the comparison of MOF-5 and 40 Ni-MOF-5, the highest moisture content of 20 Ni-MOF-5 was found at 35% RH because as we add a small amount of Ni content more spaces have become available for adsorption because the ionic size of Ni is smaller than Zn. In the case of 40 Ni-MOF-5, it might be possible that as we increase Ni content more spaces were filled with Ni due to the small atomic size of Ni, as a result smaller number of spaces were left for adsorption. Notably, 20 Ni-MOF-5 exhibited the highest adsorption capacity, suggesting that a certain degree of Ni^{2+} doping can inhibit MOF-5 intercalation. However, with the increased Ni content, intercalated structures were formed which limits the adsorption capacity. After reaching at maximum point, the value of moisture content starts decreasing might be due to after attaining the maximum point the material starts to degrade at this point and desorption occurs.

The incorporation of metal introduces electron-rich sites, vacant positions, and hierarchical pore diameter which may enhance inherent characteristics of MOFs such as higher porosity, stability, and more interaction sites for adsorption. The adsorption capacity of Ni-doped MOFs increased, but increasing the Ni content may lead to blockage of some pores due to the small size of Ni resulting in low adsorption in the

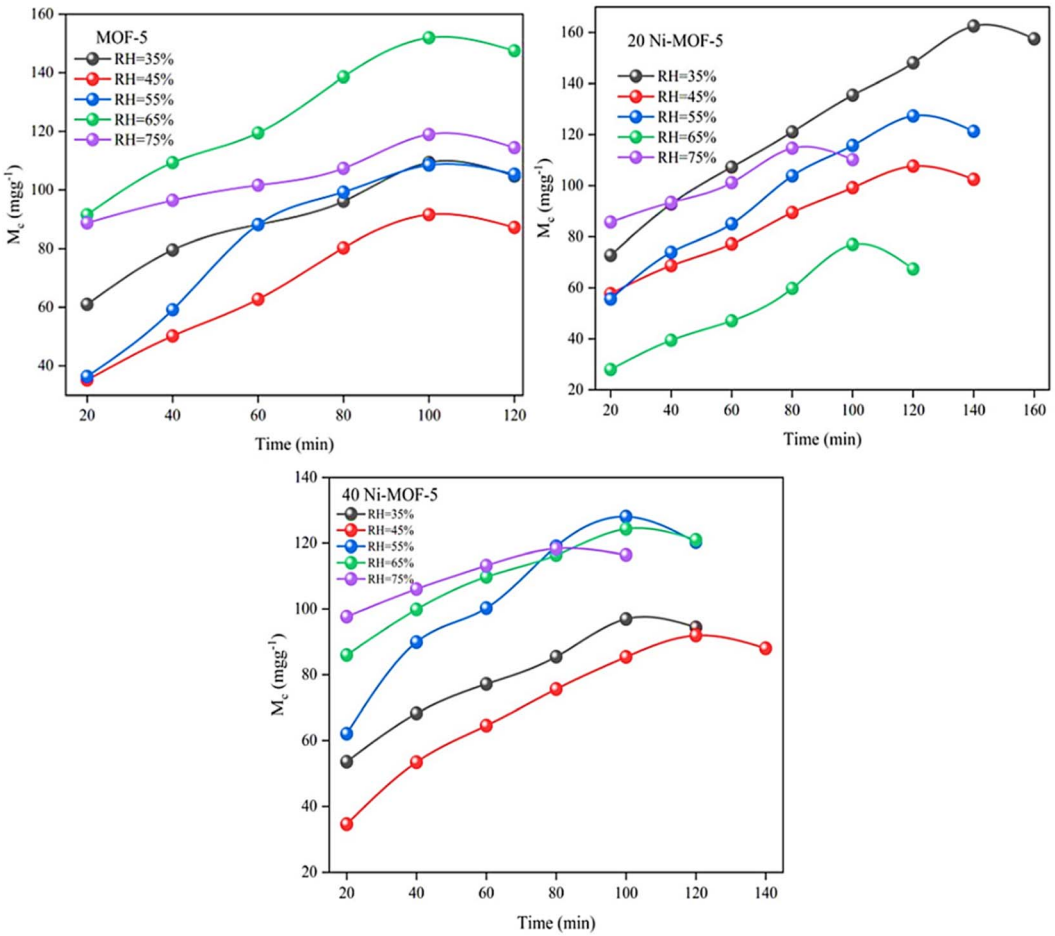

Fig. 5 Plot of M_c *versus* time for MOF-5 and its doped derivatives at different RH.

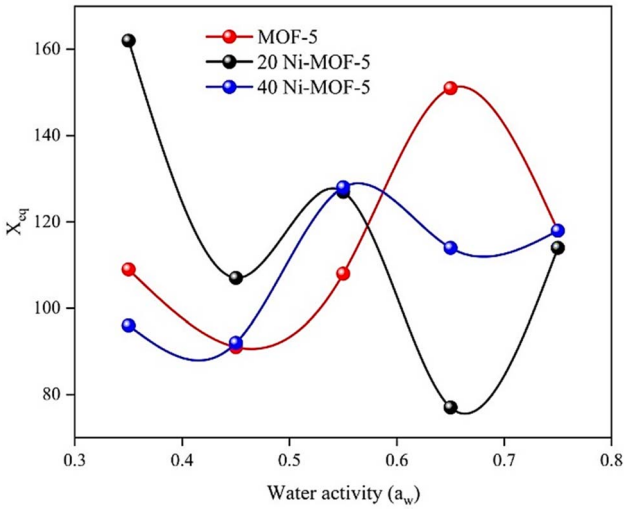

Fig. 6 X_{eq} *versus* a_w for MOF-5 and its doped derivatives.

case of 40 Ni-MOF-5. The EMC *versus* water activity (a_w) is depicted in Fig. 6. Where a_w is defined as:

$$a_w = \frac{RH\%}{100} \quad (15)$$

The water sorption data for MOF-5 and its doped derivatives at room temperature is presented in Fig. 5. The doping of nickel (Ni^{2+}) into MOF-5 changes the adsorption properties, as seen in the differences between the curves for MOF-5, 20 Ni-MOF-5, and 40 Ni-MOF-5.

The equilibrium moisture content for 20 Ni-MOF-5 shows the most variation across the water activity range, suggesting a more sensitive response to changes in water activity. The 40 Ni-MOF-5 generally exhibits higher equilibrium moisture content at intermediate water activities compared to the undoped MOF-5. MOF-5 exhibits a face-centered cubic crystal structure as demonstrated by an ideal single crystal. The fundamental component of the structure can be straightforwardly conceptualized as a cube. Each corner is constructed from a $[Zn_4O]^{6+}$ metal cluster, with each edge connected by 1,4-benzenedicarboxylate (BDC). A significant void is created within each unit cell, allowing 55–61% of the space accessible for adsorption. Ming and coworkers suggested that there are more than 20 adsorption sites available on metal culture and 12 on organic linker. There are three ways of interaction available on MOF structure. First, by directly replacing the oxygen of the M–O by oxygen of the water molecules. Second, forming a hydrogen between the hydrogen of the water molecule and oxygen of the cluster and third by forming several hydrogen bonding with MO4 cluster of the MOFs.

6.2 Adsorption isotherm models

One of the most crucial aspects of adsorption is its isotherms, which describe the interactions between the adsorbent and the adsorbate. In our study, we evaluated the effectiveness of adsorption using several isotherm models. The maximum adsorption capacity is attained when a complete monolayer of adsorbate molecules is uniformly formed on the surface of the adsorbent. The following equation represents the Langmuir model:

$$\frac{1}{Q_e} = \frac{1}{Q_{max} K_L} \frac{1}{C_e} = \frac{1}{Q_{max}} \quad (16)$$

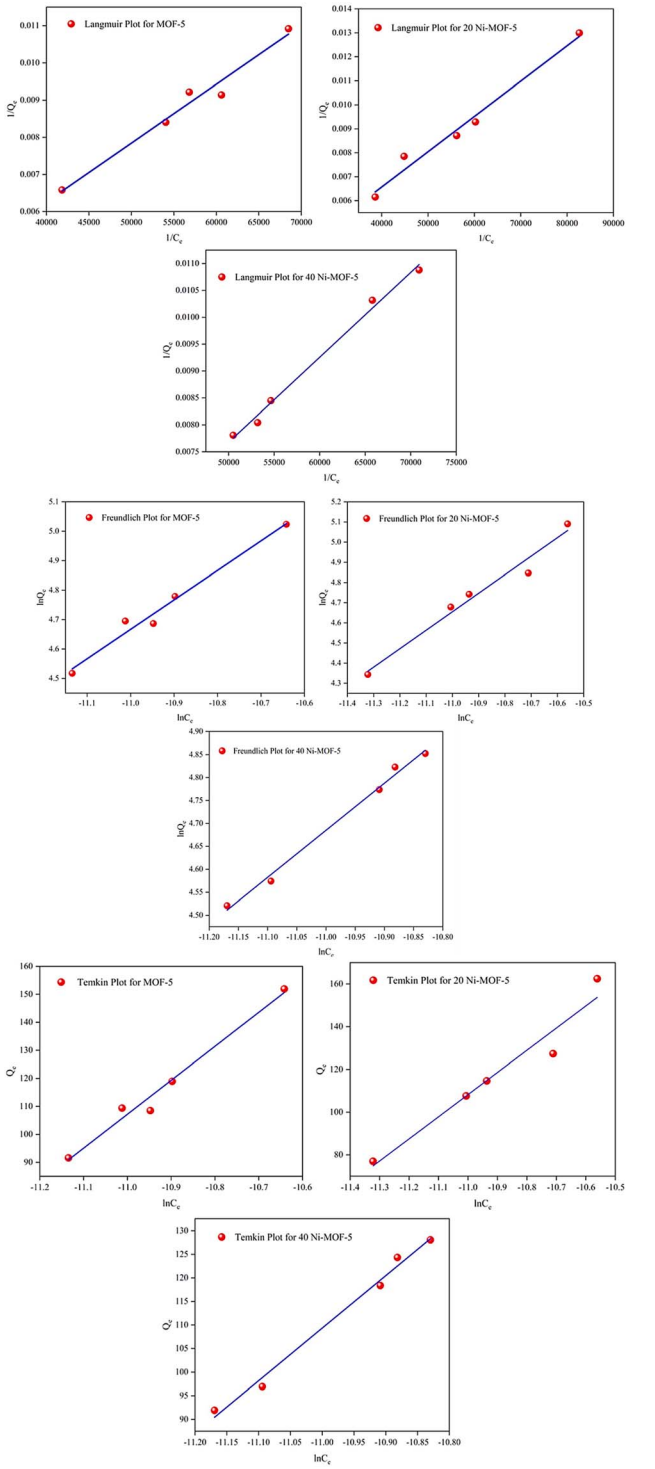

Fig. 7 Langmuir, Freundlich and Temkin isotherm models for MOF-5 and its doped derivatives.

Here, Q_e corresponds to the adsorption capacity at equilibrium (mg g^{-1}), Q_{max} defines the maximum monolayer capacity of the adsorbent (mg g^{-1}), C_e indicates the equilibrium concentration of the adsorbate in solution (mg L^{-1}), and K_L represents the Langmuir constant reflecting adsorption affinity. R_L is a factor of separation. It gives details on the type of adsorption process a material display: irreversible ($R_L = 0$), linear ($R_L = 1$), or unfavorable ($R_L > 1$).

Another type of physical adsorption known as multilayer adsorption is described by Freundlich isotherms. In this type of adsorption isotherm, there are numerous layers of adsorption and weak molecular connections. Additionally, presuming heterogeneous adsorption sites is the Freundlich isotherm. The following equation represents the Freundlich isotherm:

$$\ln Q_e = \ln k_f + \frac{1}{n} \ln C_e \quad (17)$$

The Q_e, C_e, and n stand for the Freundlich constant, k_f, the quantity of absorbed adsorbate molecule per gram of absorbent, the equilibrium concentration of the adsorbate, and the degree of linearity between the adsorbate and the adsorption process. When $n = 1$, physisorption occurs when $n > 1$, chemisorption occurs when $n < 1$, and linear adsorption occurs when $n = 1$. Temkin model suggests that the adsorption heat decreases linearly. It is assumed that the adsorbent surface possesses homogeneous binding sites with equal energy, and the adsorption process is governed by direct interactions between the adsorbate and the adsorbent. The following equation represents the Temkin model;

$$Q_e = B_T \ln A_T + B_T \ln C_e \quad (18)$$

Here, A_T represents the equilibrium binding constant, while B_T corresponds to the heat of adsorption. The magnitude of B_T is used to distinguish between physical and chemical adsorption: values of B_T greater than 8 kJ mol^{-1} indicate chemisorption, whereas values below 8 kJ mol^{-1} signify physisorption. The R_L value for MOF-5 is 0.99 and for doped derivatives is 1 which evaluates that adsorption is favorable and linear. Another aspect reflects that adsorbent has a good capacity for adsorbing the adsorbate at the initial concentration.

Fig. 7 presents the Langmuir, Freundlich and Temkin isotherm models for MOF-5 and its doped derivatives. The isotherm parameters of the applied models for MOF-5 and its doped derivatives are presented in Table 5. All materials show a value $n = 1$ or near to 1 indicating linear adsorption and chemisorption behavior. It was observed that the value of B_T is

Table 5 Parameters for Langmuir, Freundlich and Temkin isotherms

Materials	Langmuir, R^2/R_L	Freundlich, K_F/n	Temkin, A_T/B_T (kJ mol^{-1})
MOF-5	0.96/0.99	4.75/0.99	14.50/121
20 Ni-MOF-5	0.97/1.00	5.54/1.00	17.00/104
40 Ni-MOF-5	0.99/1.00	9.44/0.97	16.02/111

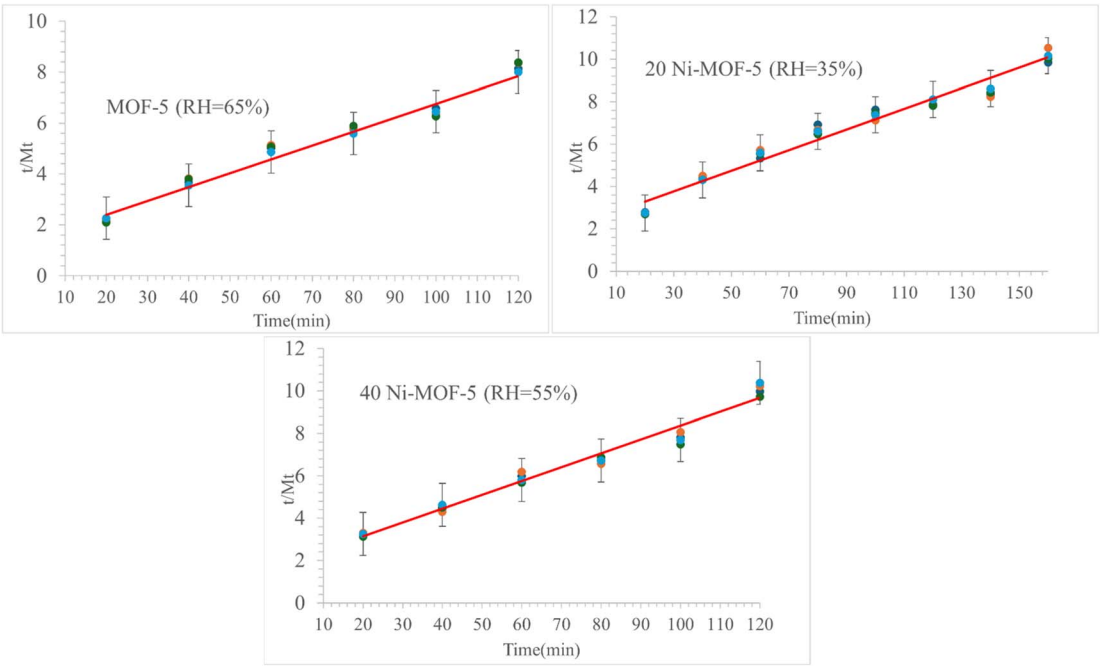

Fig. 8 Pseudo second order kinetics study on MOF-5 and its doped derivatives.

greater than 8 kJ mol^{-1} so all the synthesized materials show chemisorption behavior.

6.3 Kinetics studies

6.3.1 Pseudo 2nd order model. When t/M_t was plotted against time (t), with error bars representing standard deviation across replicates, a straight line was produced, having the values presented in Fig. 8 and Table 6. Applying the second-order kinetics model yielded a developed value for the R^2. This visualization preserves the dynamic nature of the adsorption kinetic data and also conveys variability at each point. Consequently, there is a good link between the parameters and the experimental outcomes. Additionally indicating the material's chemisorption behavior following the second-order kinetics.

Table 6 Parameters of pseudo second order kinetics model for MOF-5 and its doped derivatives

Materials	RH (%)	Slope (m)	Intercept (c)	k_2 (min^{-1})	R^2
MOF-5	65 ± 2	0.05611	1.29755	0.072	0.98
20 Ni-MOF-5	35 ± 2	0.04885	2.31099	0.112	0.97
40 Ni-MOF-5	55 ± 2	0.06369	1.90156	0.121	0.97

6.4 Thermodynamics study

To explain the thermodynamic driving force behind the adsorption process, a detailed analysis was conducted using Clausius–Clapeyron equation given below.

$$\ln a_w = -\frac{q_{st}}{R}\frac{1}{T} + C \quad (19)$$

where q_{st} is the net isosteric heat of sorption (J mol^{-1}), T is the absolute temperature, R is the general gas constant (8.314 J mol^{-1} K^{-1}) and C is the constant. The net isosteric heat of adsorption can be determined using the relation 19, by constructing a plot of ln(a_w) against 1/t as shown in Fig. 9 for MOF-5.

The entropy and Gibbs free energy can be calculated from the slope and intercept values and are given in Table 7. The calculated thermodynamic parameters strongly support the Langmuir-type adsorption process. The moderate and relatively constant value of −40.41 kJ mol^{-1} for isosteric heat is a characteristic of physisorption and suggests a uniform adsorption throughout the surface. Similarly, the negative entropy change (−0.2914 kJ mol^{-1}) indicate reduced molecular randomness upon absorption indicating a localized binding at surface favoring Langmuir model. The negative free energy further

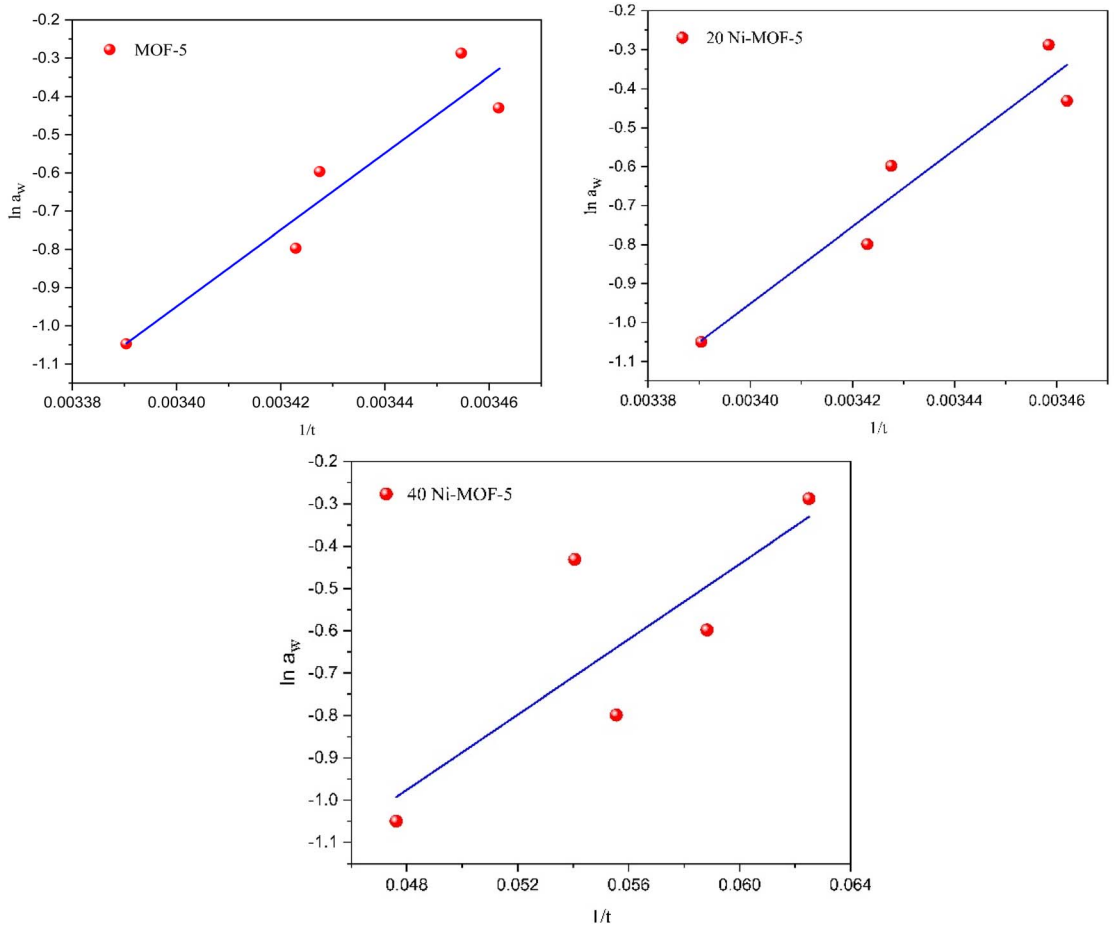

Fig. 9 ln a_w *versus* 1/t for MOF-5 and its doped derivatives.

Table 7 Thermodynamic parameters for MOF-5

	MOF-5	20 Ni-MOF-5	40 Ni-MOF-5
Isosteric heat of adsorption (kJ mol^{-1})	−40.41	−38.00	−40.23
Entropy (kJ mol^{-1})	−0.291	−0.287	−0.85
Gibbs free energy (kJ mol^{-1})	−2.56	−2.57	−2.56

favors the spontaneous nature of adsorption and a small value validates physisorption.

7. Conclusion

The effective synthesis of MOF-5 and its nickel-doped derivatives was achieved with the aim of enhancing the hydrolytic stability of the framework. This advancement holds particular significance in addressing global water scarcity challenges. Comprehensive characterization using XRD, FTIR, EDX, and SEM confirmed the successful formation, crystallinity, and structural integrity of the synthesized materials. Among the tested samples, pristine MOF-5 exhibited a maximum adsorption capacity of 151 mg g^{-1} at 65% RH, while 20% Ni-MOF-5 demonstrated an enhanced capacity of 162 mg g^{-1} at 35% RH. In comparison, 40% Ni-MOF-5 recorded an adsorption capacity of 142 mg g^{-1} at 55% RH. The incorporation of nickel into the MOF-5 framework not only improved water uptake performance but also contributed to enhanced structural stability. The thermodynamic parameters affirm that adsorption process is spontaneous and exothermic, governed primarily by physisorption. Kinetic and thermodynamic analyses further confirmed the predominance of chemisorption mechanisms, supporting the materials' potential for efficient water capture and retention. In general, these findings highlight the promise of Ni-doped MOF-5 materials as sustainable and effective adsorbents for water harvesting and humidity control in resource-limited environments.

Author contributions

Momna Aziz: conceived and designed the experiments, performed the experiments, analyzed the data, prepared figures and/or tables, writing-original draft. Raouf Hassan: reviewing, validation, data acquisition, and funding. Muhammad Saeed-Ul-Hassan: conceived and designed the experiments, and prepared figures and/or tables. Muhammad Ehtisham: conceived and designed the experiments, validation, and data acquisition. Mansour S. Almatawa: reviewing, validation, data acquisition, and funding. Ahmad K. Badawi: authored or reviewed drafts of the article, editing, validation, and approved the final draft. Bushra Ismail: supervision, provided materials, conceived and designed the experiments, analyzed the data, authored or reviewed drafts of the article, validation, and approved the final draft.

Conflicts of interest

There are no conflicts to declare.

Data availability

All the data is provided in the manuscript and SI files. See DOI: https://doi.org/10.1039/d5ra05257b.

Funding statement

This work was supported and funded by the Deanship of Scientific Research at Imam Mohammad Ibn Saud Islamic University (IMSIU) (grant number IMSIU-DDRSP2502).

Acknowledgements

The authors extend their appreciation to the Deanship of Scientific Research at Imam Mohammad Ibn Saud Islamic University (IMSIU) for funding this research work (grant number IMSIU-DDRSP2502).

References

1 B. Al Alwan, B. Ismail, A. El Jery and A. K. Badawi, State-of-the-art strategies for microplastics mitigation in aquatic environments: identification, technological innovations, and prospects for advancement, *J. Water Process Eng.*, 2024, **61**, 105336.
2 B. Wang, X. Zhou, Z. Guo and W. Liu, Recent advances in atmosphere water harvesting: design principle, materials, devices, and applications, *Nano Today*, 2021, **40**, 101283.
3 X. Huang, Q. Qin, Q. Ma and B. Wang, Atmospheric Water Harvesting with Metal-Organic Frameworks and Their Composites: From Materials to Devices, *Water*, 2022, **14**(21), 3487.
4 K. Yang, T. Pan, Q. Lei, X. Dong, Q. Cheng and Y. Han, A Roadmap to Sorption-Based Atmospheric Water Harvesting: From Molecular Sorption Mechanism to Sorbent Design and System Optimization, *Environ. Sci. Technol.*, 2021, **55**(10), 6542–6560.
5 R. Hassan, A. E. Alluqmani and A. K. Badawi, An eco-friendly solution for greywater treatment via date palm fiber filter, *Desalin. Water Treat.*, 2024, **317**, 100163.
6 G. Tian, C. Fu and Z. Guo, Metal-organic framework-based composite adsorbents for atmospheric water harvesting: materials and devices, *Mater. Today*, 2025, **83**, 307–330.
7 A. K. Badawi and R. Hassan, Optimizing sludge extract reuse from physico-chemical processes for zero-waste discharge: a critical review, *Desalin. Water Treat.*, 2024, **319**, 100527.
8 M. Ahtasham Iqbal, S. Akram, S. Khalid, B. Lal, S. U. Hassan, R. Ashraf, *et al.*, Advanced photocatalysis as a viable and

sustainable wastewater treatment process: a comprehensive review, *Environ. Res.*, 2024, **253**, 118947.
9 Z. Zhang, Y. Wu, L. Luo, G. Li, Y. Li and H. Hu, Application of disk tube reverse osmosis in wastewater treatment: a review, *Sci. Total Environ.*, 2021, **792**, 148291.
10 F. Bagheri, Performance investigation of atmospheric water harvesting systems, *Water Resour. Ind.*, 2018, **20**, 23–28.
11 Y. Hu, Z. Ye and X. Peng, Metal-organic frameworks for solar-driven atmosphere water harvesting, *Chem. Eng. J.*, 2023, **452**, 139656.
12 J. Wang, J. Song and Q. Zhou, In situ-growth of Fe_2S_3 ultrathin layer on CdS nanorod through cation-exchange for efficient photocatalytic degradation of organic pollutants under visible light coupled oxidant activation, *Desalin. Water Treat.*, 2024, **319**, 100434.
13 A. LaPotin, H. Kim, S. R. Rao and E. N. Wang, Adsorption-Based Atmospheric Water Harvesting: Impact of Material and Component Properties on System-Level Performance, *Acc. Chem. Res.*, 2019, **52**(6), 1588–1597.
14 M. J. Kalmutzki, C. S. Diercks and O. M. Yaghi, Metal–Organic Frameworks for Water Harvesting from Air, *Adv. Mater.*, 2018, **30**(37), 1704304.
15 H. Jarimi, R. Powell and S. Riffat, Review of sustainable methods for atmospheric water harvesting, *Int. J. Low-Carbon Technol.*, 2020, **15**(2), 253–276.
16 M. Bilal, M. Sultan, T. Morosuk, W. Den, U. Sajjad, M. M. A. Aslam, *et al.*, Adsorption-based atmospheric water harvesting: a review of adsorbents and systems, *Int. Commun. Heat Mass Transfer*, 2022, **133**, 105961.
17 X. Zhou, H. Lu, F. Zhao and G. Yu, Atmospheric Water Harvesting: A Review of Material and Structural Designs, *ACS Mater. Lett.*, 2020, **2**(7), 671–684.
18 M. Azeem, M. T. Noman, J. Wiener, M. Petru and P. Louda, Structural design of efficient fog collectors: a review, *Environ. Technol. Innovation*, 2020, **20**, 101169.
19 N. Hanikel, M. S. Prévot and O. M. Yaghi, MOF water harvesters, *Nat. Nanotechnol.*, 2020, **15**(5), 348–355.
20 M. O. Alhurmuzi, M. Danışmaz and O. A. Zainal, Investigation of silica gel performance on potable water harvesting from ambient air using a rotatable apparatus with a solar tracking system, *Desalin. Water Treat.*, 2023, **304**, 12–24.
21 T. Z. Wasti, M. Sultan, M. Aleem, U. Sajjad, M. Farooq, H. M. Raza, *et al.*, An overview of solid and liquid materials for adsorption-based atmospheric water harvesting, *Adv. Mech. Eng.*, 2022, **14**(3), 16878132221082768.
22 F. Deng, C. Xiang, C. Wang and R. Wang, Sorption-tree with scalable hygroscopic adsorbent-leaves for water harvesting, *J. Mater. Chem. A*, 2022, **10**(12), 6576–6586.
23 P. A. Kallenberger and M. Fröba, Water harvesting from air with a hygroscopic salt in a hydrogel–derived matrix, *Commun. Chem.*, 2018, **1**(1), 28.
24 A. K. Sleiti, H. Al-Khawaja, H. Al-Khawaja and M. Al-Ali, Harvesting water from air using adsorption material – prototype and experimental results, *Sep. Purif. Technol.*, 2021, **257**, 117921.
25 F. Zhao, X. Zhou, Y. Liu, Y. Shi, Y. Dai and G. Yu, Super Moisture-Absorbent Gels for All-Weather Atmospheric Water Harvesting, *Adv. Mater.*, 2019, **31**(10), 1806446.
26 B. Lian, S. De Luca, Y. You, S. Alwarappan, M. Yoshimura, V. Sahajwalla, *et al.*, Extraordinary water adsorption characteristics of graphene oxide, *Chem. Sci.*, 2018, **9**(22), 5106–5111.
27 A. E. Thorarinsdottir and T. D. Harris, Metal–Organic Framework Magnets, *Chem. Rev.*, 2020, **120**(16), 8716–8789.
28 N. L. Rosi, J. Eckert, M. Eddaoudi, D. T. Vodak, J. Kim, M. O'Keeffe, *et al.*, Hydrogen Storage in Microporous Metal-Organic Frameworks, *Science*, 2003, **300**(5622), 1127–1129.
29 C. Jiang, X. Wang, Y. Ouyang, K. Lu, W. Jiang, H. Xu, *et al.*, Recent advances in metal–organic frameworks for gas adsorption/separation, *Nanoscale Adv.*, 2022, **4**(9), 2077–2089.
30 Y. Zhang, X. Yu, Y. Hou, C. Liu, G. Xie and X. Chen, Current research status of MOF materials for catalysis applications, *Mol. Catal.*, 2024, **555**, 113851.
31 W. Cheng, X. Tang, Y. Zhang, D. Wu and W. Yang, Applications of metal-organic framework (MOF)-based sensors for food safety: enhancing mechanisms and recent advances, *Trends Food Sci. Technol.*, 2021, **112**, 268–282.
32 Z. Wang, X. Yue and Q. Xiang, MOFs-based S-scheme heterojunction photocatalysts, *Coord. Chem. Rev.*, 2024, **504**, 215674.
33 Y. Peng, J. Xu, J. Xu, J. Ma, Y. Bai, S. Cao, *et al.*, Metal-organic framework (MOF) composites as promising materials for energy storage applications, *Adv. Colloid Interface Sci.*, 2022, **307**, 102732.
34 H. Furukawa, F. Gándara, Y. B. Zhang, J. Jiang, W. L. Queen, M. R. Hudson, *et al.*, Water Adsorption in Porous Metal–Organic Frameworks and Related Materials, *J. Am. Chem. Soc.*, 2014, **136**(11), 4369–4381.
35 H. Kim, S. Yang, S. R. Rao, S. Narayanan, E. A. Kapustin, H. Furukawa, *et al.*, Water harvesting from air with metal-organic frameworks powered by natural sunlight, *Science*, 2017, **356**(6336), 430–434.
36 Y. Feng, T. Ge, B. Chen, G. Zhan and R. Wang, A regulation strategy of sorbent stepwise position for boosting atmospheric water harvesting in arid area, *Cell Rep. Phys. Sci.*, 2021, **2**(9), 100561.
37 N. Hanikel, M. S. Prévot, F. Fathieh, E. A. Kapustin, H. Lyu, H. Wang, *et al.*, Rapid Cycling and Exceptional Yield in a Metal-Organic Framework Water Harvester, *ACS Cent. Sci.*, 2019, **5**(10), 1699–1706.
38 Z. Zheng, H. L. Nguyen, N. Hanikel, K. K. Y. Li, Z. Zhou, T. Ma, *et al.*, High-yield, green and scalable methods for producing MOF-303 for water harvesting from desert air, *Nat. Protoc.*, 2023, **18**(1), 136–156.
39 G. Fu, P. Wu, X. Huai and L. Wang, *Microwave Assisted Synthesis of Cr-doped UiO-66 with Enhanced Water Adsorption Capacity*, 2022, Available from: **https://www.energy-proceedings.org/?p=9472**, accessed 26 August 2025.

40 B. Chen, X. Wang, Q. Zhang, X. Xi, J. Cai, H. Qi, *et al.*, Synthesis and characterization of the interpenetrated MOF-5, *J. Mater. Chem.*, 2010, **20**(18), 3758.

41 K. K. Gangu, S. Maddila and S. B. Jonnalagadda, The pioneering role of metal–organic framework-5 in ever-growing contemporary applications – a review, *RSC Adv.*, 2022, **12**(22), 14282–14298.

42 A. M. P. Peedikakkal and I. H. Aljundi, Upgrading the Hydrogen Storage of MOF-5 by Post-Synthetic Exchange with Divalent Metal Ions, *Appl. Sci.*, 2021, **11**(24), 11687.

43 R. Saini, P. Wadhwa, K. Jain, M. Pathak, P. Singh, R. K. Dhaka, *et al.*, Enhancement of electrochemical energy storage performance of MOF-5 and Eucalyptus plant bark derived rGO composite, *Phys. Scr.*, 2025, **100**(3), 035959.

44 C. Chen, L. Meng, M. R. Alalouni, X. Dong, Z. Wu, S. Zuo, *et al.*, Ultra-Highly Active Ni-Doped MOF-5 Heterogeneous Catalysts for Ethylene Dimerization, *Small*, 2023, **19**(25), 2301235.

45 A. A. Vodyashkin, A. V. Sergorodceva, P. Kezimana and Y. M. Stanishevskiy, Metal-Organic Framework (MOF)—A Universal Material for Biomedicine, *Int. J. Mol. Sci.*, 2023, **24**(9), 7819.

46 S. Jamali, M. Kazemzad, N. Naderi, M. J. Eshraghi and M. M. Sabzehmeidani, Preparation of hierarchical MOF-5 films using morphology controlled ZnO coatings for temperature dependent optical sensors application, *Mater. Chem. Phys.*, 2023, **304**, 127775.

47 A. A. Mohammadi, S. Moghanlo, M. S. Kazemi, S. Nazari, S. K. Ghadiri, H. N. Saleh, *et al.*, Comparative removal of hazardous cationic dyes by MOF-5 and modified graphene oxide, *Sci. Rep.*, 2022, **12**(1), 15314.

48 P. Chen, Z. Zhu, Z. Liu, F. Liang, X. Zhu, Z. Bin, *et al.*, Efficient removal of ciprofloxacin from water by BiOX/GaMOF S-scheme heterojunction: a synergistic effect of adsorption and photocatalysis, *Chem. Eng. J.*, 2025, **506**, 159689.

49 J. G. Vitillo, L. Regli, S. Chavan, G. Ricchiardi, G. Spoto, P. D. C. Dietzel, *et al.*, Role of Exposed Metal Sites in Hydrogen Storage in MOFs, *J. Am. Chem. Soc.*, 2008, **130**(26), 8386–8396.

50 K. M. Choi, H. M. Jeong, J. H. Park, Y. B. Zhang, J. K. Kang and O. M. Yaghi, Supercapacitors of Nanocrystalline Metal–Organic Frameworks, *ACS Nano*, 2014, **8**(7), 7451–7457.

51 J. M. Yang, Q. Liu and W. Y. Sun, Shape and size control and gas adsorption of Ni(II)-doped MOF-5 nano/microcrystals, *Microporous Mesoporous Mater.*, 2014, **190**, 26–31.

52 J. A. Botas, G. Calleja, M. Sánchez-Sánchez and M. G. Orcajo, Cobalt Doping of the MOF-5 Framework and Its Effect on Gas-Adsorption Properties, *Langmuir*, 2010, **26**(8), 5300–5303.

53 H. Li, W. Shi, K. Zhao, H. Li, Y. Bing and P. Cheng, Enhanced Hydrostability in Ni-Doped MOF-5, *Inorg. Chem.*, 2012, **51**(17), 9200–9207.

54 G. Chen, J. Luo, M. Cai, L. Qin, Y. Wang, L. Gao, *et al.*, Investigation of Metal-Organic Framework-5 (MOF-5) as an Antitumor Drug Oridonin Sustained Release Carrier, *Molecules*, 2019, **24**(18), 3369.

55 J. J. Gulicovski, L. S. Čerović and S. K. Milonjić, Point of Zero Charge and Isoelectric Point of Alumina, *Mater. Manuf. Processes*, 2008, **23**(6), 615–619.

56 R. Ragadhita and A. B. D. Nandiyanto, How to Calculate Adsorption Isotherms of Particles Using Two-Parameter Monolayer Adsorption Models and Equations, *Indones. J. Sci. Technol.*, 2021, **6**(1), 205–234.

57 J. Wang and X. Guo, Adsorption kinetic models: physical meanings, applications, and solving methods, *J. Hazard. Mater.*, 2020, **390**, 122156.

58 Z.-s. Zhang, X.-d. Li, H.-j. Jia and Y.-l. Liu, Moisture sorption isotherms and thermodynamic properties of tiger nuts: an oil-rich tuber, *LWT*, 2022, **167**, 113866.

59 C. Chinglenthoiba, G. Mahadevan, J. Zuo, T. Prathyumnan and S. Valiyaveettil, Conversion of PET Bottle Waste into a Terephthalic Acid-Based Metal-Organic Framework for Removing Plastic Nanoparticles from Water, *Nanomaterials*, 2024, **14**(3), 257.

60 R. A. Shaukat, Q. M. Saqib, J. Kim, H. Song, M. U. Khan, M. Y. Chougale, *et al.*, Ultra-robust tribo- and piezo-electric nanogenerator based on metal organic frameworks (MOF-5) with high environmental stability, *Nano Energy*, 2022, **96**, 107128.

61 H. Aykac Ozen and B. Ozturk, Gas separation characteristic of mixed matrix membrane prepared by MOF-5 including different metals, *Sep. Purif. Technol.*, 2019, **211**, 514–521.

62 A. Parkash, Synthesis of Bimetal Doped Metal-Organic Framework (MOF-5): An Electrocatalyst with Low Noble Metal Content and High Electrochemical Activity, *ECS J. Solid State Sci. Technol.*, 2020, **9**(7), 075002.